# Supplementary material for:

# A comprehensive evaluation of enhanced temperature influence on gas and aerosol chemistry in the lamp-enclosed oxidation flow reactor (OFR) system

5  Tianle Pan[1,2,3,4,5], Andrew T. Lambe[6], Weiwei Hu[1,2,4,5], Yicong He[7,a], Minghao Hu[8], Huaishan Zhou[1,2,3,4,5], Xinming Wang[1,2,4,5], Qingqing Hu[9], Hui Chen[9], Yue Zhao[10], Yuanlong Huang[11], Doug R. Worsnop[6,12], Zhe Peng[13,14], Melissa A. Morris[13,14], Douglas A. Day[13,14], Pedro Campuzano-Jost[13,14], Jose-Luis Jimenez[13,14], Shantanu H. Jathar[6]

[1]State Key Laboratory of Organic Geochemistry, Guangzhou Institute of Geochemistry, Chinese Academy of Sciences,
10  Guangzhou 510640, China
[2]CAS Center for Excellence in Deep Earth Science, Guangzhou, 510640, China
[3]Chinese Academy of Sciences University, Beijing 100049, China
[4]Guangdong-Hong Kong-Macao, Joint Laboratory for Environmental Pollution and Control, Guangzhou Institute of Geochemistry, Chinese Academy of Science, Guangzhou 510640, China
15  [5]Guangdong Provincial Key Laboratory of Environmental Protection and Resources Utilization, Chinese Academy of Science, Guangzhou 510640, China
[6]Aerodyne Research Inc., Billerica, Massachusetts, 01821, United States
[7]Department of Mechanical Engineering, Colorado State University, Fort Collins, Colorado 80523, United States
[8]China-UK Low Carbon College, Shanghai Jiao Tong University, Shanghai, 201306, China
20  [9]Key Laboratory of Organic Compound Pollution Control Engineering, School of Environmental and Chemical Engineering, Shanghai University, 200444, Shanghai, China
[10]School of Environmental Science and Engineering, Shanghai Jiao Tong University, Shanghai, 200240, China
[11]Department of Environmental Science and Engineering, California Institute of Technology, Pasadena, California 91125, United States
25  [12]Institute for Atmospheric and Earth System Research (INAR) / Physics, Faculty of Science, University of Helsinki, Helsinki, 00014, Finland
[13]Cooperative Institute for Research in the Environmental Sciences (CIRES), University of Colorado at Boulder, Boulder, Colorado, 80309, United States
[14]Department of Chemistry, University of Colorado at Boulder, Boulder, Colorado 80309, United States
30  [a]now at: State Key Joint Laboratory of Environmental Simulation and Pollution Control, School of Environment, Tsinghua University, Beijing 100084, China

*Correspondence to*: Weiwei Hu (weiweihu@gig.ac.cn)

## S1 Supply power for Light Source and BHK lamps

For the UV lamps from Light Source Inc., the supply power (8.9 W) was calculated as 185 mA/425 mA $\times$ 21 W, where 185 mA is the measured current controlled by the ballast at 10 VAC (full) output; 425 mA and 21 W are the manufacturer specified current and power. For BHK lamps, the supply power (6.3 W) was measured directly with a Kill-A-Watt sensor on the outlet of the lamp controller box at full AC output.

## S2 Calculation of the heating energy in OFR

For the temperature measured for a lamp control voltage of 10 V (full AC power) and flow rate of 5 L min$^{-1}$ (Fig. 4), we calculated the fraction of heating energy transferred from the UV lamps to the gas inside the OFR ($f_g$), the $N_2$ purge gas ($f_{N_2}$), and the OFR tube wall ($f_s$). Results were estimated on the assumption that all the electrical input power of the lamps was finally converted into heat, which led to the rise in temperature. We did not consider the heat exchange between the gas inside the OFR, $N_2$ purge gas, and OFR surface. The energy of gas inside the OFR (or $N_2$ inside the lamp sleeves) would be lost due to the gas (or $N_2$) entering and leaving the OFR (or lamps sleeve), depending on the flow rate and the temperature of the ambient gas (or $N_2$,0.2 and 20 L min$^{-1}$). Also, the OFR surface dissipate heat to the ambient air. Based on the timeseries of measured temperature in Fig. 4, the $f_g$, $f_s$, and $f_{N_2}$ could be calculated as follows:

$$f_g = \frac{Q_g}{Q_{Total}} = \frac{C_g \times M_g \times \Delta T_{i-(i-1)} + C_g \times m_g \times \Delta T_{i-a}}{Q_{Total}} \quad (1)$$

$$f_s = \frac{Q_s}{Q_{Total}} = \frac{C_s \times M_s \times \Delta T_{j-(j-1)} + F \times A \times \Delta T_{j-a}}{Q_{Total}} \quad (2)$$

$$f_{N_2} = \frac{Q_{N_2}}{Q_{Total}} = \frac{C_{N_2} \times M_{N_2} \times \Delta T_{k-(k-1)} + C_{N_2} \times m_{N_2} \times \Delta T_{k-a}}{Q_{Total}} \quad (3)$$

Where $Q_g$, $Q_s$, and $Q_{N_2}$ were the energy in 1 second of lamps allocated to the gas inside OFR, surface of OFR and $N_2$ purge gas, respectively; $Q_{Total}$ is the total energy from 4 lamps in 1 s (35.6 J, 8.9 W for each lamp at full VAC). $C_g$, $C_s$ and $C_{N_2}$ were the specific heat capacity of gas (1.005 kJ kg$^{-1}$ K$^{-1}$ at 300 K), OFR surface (aaluminum, 0.879 kJ kg$^{-1}$ K$^{-1}$ at 293 K) and $N_2$ (1.038 kJ kg$^{-1}$ K$^{-1}$ at 298 K); $M_g$, $M_s$ and $M_{N_2}$ were the mass of gas inside OFR, OFR surface, and $N_2$ in lamp sleeves; $\Delta T_{i-(i-1)}$ was the temperature difference between i$^{th}$ and (i-1)$^{th}$ second for gas inside OFR. $\Delta T_{j-(j-1)}$ and $\Delta T_{k-(k-1)}$ were similar, for the temperature of OFR surface and $N_2$ purge gas; $m_g$ was the mass of gas entered or left OFR in one second; $\Delta T_{i-a}$ was the temperature difference between the gas left OFR at i$^{th}$ second and ambient air; $F$ was the Heat dissipation area for OFR surface; $A$ was the heat transfer coefficient (3.48 J m$^{-2}$ s$^{-1}$ K$^{-1}$) and $\Delta T_{j-a}$ was the temperature difference between the OFR surface at j$^{th}$

second and ambient air; $m_{N_2}$ was the mass entered or left lamps sleeve in one second; $\Delta T_{k-a}$ was the temperature difference between the $N_2$ left lamps sleeve at $k^{th}$ second and ambient air. Results were shown in Fig. S8.

**S3 Calculation of the Richardson number**

65    The Richardson number, a dimensionless number that represents the ratio of buoyancy term to flow shear term, can be calculated as follow (Holman, 2010; Huang et al., 2017):

$$R_i = \frac{g\beta D^3 \Delta T/\nu^2}{(\rho U_{avg} D/\mu)^2} \sim \frac{gD}{TU_{avg}^2}\Delta T \qquad (4)$$

where g is the gravitational acceleration (9.78 m s$^{-2}$), $\beta$ is the thermal expansion coefficient of air (T$^{-1}$ for ideal gases), D is the diameter of the flow tube (202 mm), $T$ is the temperature at centerline (39 °C), $\Delta T$ is the temperature difference between the

70    centerline and tube wall (4 °C), $\nu$ is the kinematic viscosity of air (m$^2$ s$^{-1}$), $\rho$ is the density of air (kg m$^{-3}$), $U_{avg}$ is the average velocity on the cross-section of the flow tube (m s$^{-1}$), calculated based on the flow rate (5 L min$^{-1}$) and D, $\mu$ is the dynamic viscosity (N s m$^{-2}$). When Ri<0.1, the natural convection is negligible; when Ri>10, the forced convection is negligible, and the buoyancy forces may lead to flow bifurcation and recirculation (Huang et al., 2017).

75    **Table S1: Temperature sensors used in temperature measurement.**

| Temperature sensors | Model | Manufacturer |
| --- | --- | --- |
| OFR RH/T sensor | Sensirion SHT21 | Sensirion AG |
| Vaisala | HMT130 | Vaisala Inc. |
| Thermocouple | TM-902C, type K | Shenzhen APUHUA Electronic Technology CO. LTD |
| CEM | DT-83 | Shenzhen EVERBEST machinery industry, CO, LTD. |

**Table S2: Detailed parameters of OFR temperature experiments.**

| Exp. | Flow rate (L min^{-1}) | Control Voltage (V) | Lamps [1] (num. of lamps×lamp type) | Mesh screen [2] | OFR sensor Position [3] | Position of Probe within OFR [4] | Temp. of surface | Temp. of exhaust |
|---|---|---|---|---|---|---|---|---|
| 1 | 5 | 5 | 4 × 185 covered | Back | In backplate | Vertical and horizontal at different depth | / [5] | / |
| 2 | 5 | 10/6/5/4/2 | 4 × 185 covered | Back | In backplate | Different depth from the inlet in the center | / | / |
| 3 | 3/5/7 | 5 | 4 × 185 covered | Back | In backplate | Different depth from the inlet in the center | / | / |
| 4 | 5 | 10 | 4 × 185 covered | Back | In backplate | 300 mm from the inlet in the center | Measured | / |
| 5 | 5 | 10-6-5-4-2-0 [6] | 4 ×185 covered | Back | In backplate | 300 mm from the inlet in the center | Measured | Measured |
| 6 | 5 | 10-6-5-4-2-0 | 2 ×185 covered | Back | In backplate | 300 mm from the inlet in the center | Measured | / |
| 7 | 5 | 10-6-5-4-2-0 | 2 ×185 covered | / | 300 mm from inlet | 300 mm from the inlet in the center | Measured | Measured |
| 8 | 5 | 10-6-5-4-2-0 | 4 × 185 | Back | In backplate | 300 mm from the inlet in the center | / | / |
| 9 | 5 | 10-6-5-4-2-0 | 2 × 254 | Back | In backplate | 300 mm from the inlet in the center | / | / |
| 10 | 5 | 10-6-5-4-2-0 | 4 ×185 covered | Front | 300 mm from inlet | / | Measured | Measured |
| 11 | 5 | 10-6-5-4-2-0 | 2 ×185 covered | Front | 300 mm from inlet | / | Measured | Measured |
| 12 | 5 | 10-2-6-3-5-0 | 4 ×185 covered | Back | In backplate | 300 mm from the inlet in the center | / | / |

[1] Three types of lamps were used (Figure S2). '185 covered' transmits both 185 and 254 nm radiation, with 80% surface covered with heat-shrink tubes. Lamps of '185' are the same type as '185 covered', but without covering. The lamp of '254' transmits only 254 nm radiation and is not covered.

[2] Two mesh screens are set inside OFR, one near the inlet (Front) and one near the outlet (Back).

[3] The OFR sensor is set in the backplate by default, as shown in Fig. S1.

[4] Extending the external temperature sensor into OFR from the inlet (so the 'Front' mesh screen must be removed). 4 depths were measured for Exp.1-3 (100, 200, 300, and 400 mm from the inlet, respectively)

[5] '/' means no installation or no measurement.

[6] Each voltage was set to last for 16 min.

**Table S3: SOM parameters used in this study.**

| precursor | VOC surrogate | NOx | $m_{frag}$ | $\Delta LVP$ | $p_1$ | $p_2$ | $p_3$ | $p_4$ | HOM yield[1] | reference |
|---|---|---|---|---|---|---|---|---|---|---|
| **dodecane** | dodecane | low | 2 | 1.83 | 0.999 | 0.001 | 0.001 | 0.001 | | Cappa et al. (2013) |
| | | high | 0.2627 | 1.4629 | 0.9657 | 0.0010 | 0.0020 | 0.0314 | | Loza et al. (2014) |
| **α-pinene** | α-pinene | low | 0.305 | 1.97 | 0.419 | 0.426 | 0.140 | 0.014 | 0.44% | Chhabra et al. (2011) |
| | | high | 0.1312 | 1.9139 | 0.5991 | 0.2923 | 0.1079 | 0.0007 | 0.44% | Chhabra et al. (2011) |
| **toluene** | toluene | low | 1.31 | 1.77 | 0.185 | 0.001 | 0.002 | 0.812 | 0.1% | Zhang et al. (2014) |
| | | high | 1.3064 | 1.4169 | 0.5634 | 0.3413 | 0.0016 | 0.0937 | 0.1% | Zhang et al. (2014) |
| **m-xylene** | m-xylene | low | 1.08 | 2.05 | 0.102 | 0.001 | 0.878 | 0.019 | 1.7% | Ng et al. (2007) |
| | | high | 0.0736 | 1.4601 | 0.1418 | 0.2971 | 0.4571 | 0.1040 | 1.7% | Ng et al. (2007) |

[1] Values are obtained in Bianchi et al. (2019).

90  **Table S4: The modeled variation of SOA yield per temperature (K). The concentration of organic aerosol is 15 µg m$^{-3}$ for all cases. The range of model temperature is 20-40 °C.**

| precursors | NOx | $H_i^{vap}$ evaporation enthalpy (kJ mol$^{-1}$) | | | |
| --- | --- | --- | --- | --- | --- |
| | | Equation[1] | 50 | 100 | 150 |
| dodecane | high | 0.0041-0.0052 | 0.0019-0.0022 | 0.0036-0.0050 | 0.0053-0.0095 |
| | low | 0.0062-0.0074 | 0.0026-0.0029 | 0.0053-0.0070 | 0.0078-0.010 |
| α-pinene | high | 0.0087-0.0089 | 0.0037-0.0039 | 0.0077-0.0088 | 0.011-0.015 |
| | low | 0.011-0.013 | 0.0041-0.0053 | 0.0091-0.013 | 0.01-0.011 |
| toluene | high | 0.0060-0.0068 | 0.0023-0.0026 | 0.0050-0.0063 | 0.0075-0.010 |
| | low | 0.0083-0.023 | 0.0044-0.0068 | 0.0077-0.018 | 0.0095-0.030 |
| m-xylene | high | 0.0049-0.099 | 0.0025-0.0039 | 0.0045-0.0094 | 0.0064-0.016 |
| | low | 0.0078-0.018 | 0.0043-0.0063 | 0.0073-0.015 | 0.0091-0.023 |

[1] The equation is taken from Epstein et al. (2010), $H_i^{vap} = -11 \times \log C_{i,ref}^* + 131$.

(1) Mesh screen

(2) Center inlet and hexagon nut

(3) Aerosol outlet

(4) Irradiance sensor

(5) Primary Temp&RH sensor

(6) Ring flow manifold and gas outlet
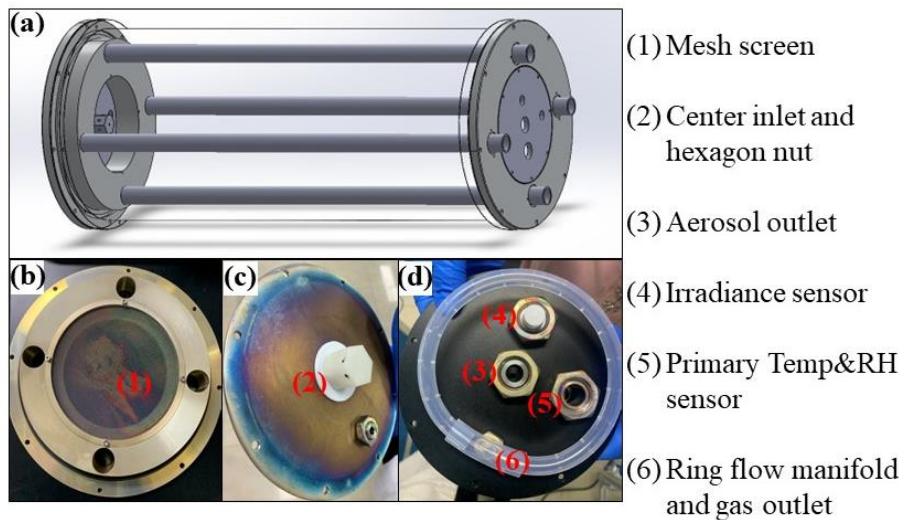
**Figure S1: Schematic diagram of (a) OFR and UV lamps and photographs of (b) mesh screen near the inlet, (c) inlet and hexagon nut and (d) outlets and sensors of OFR.**

100
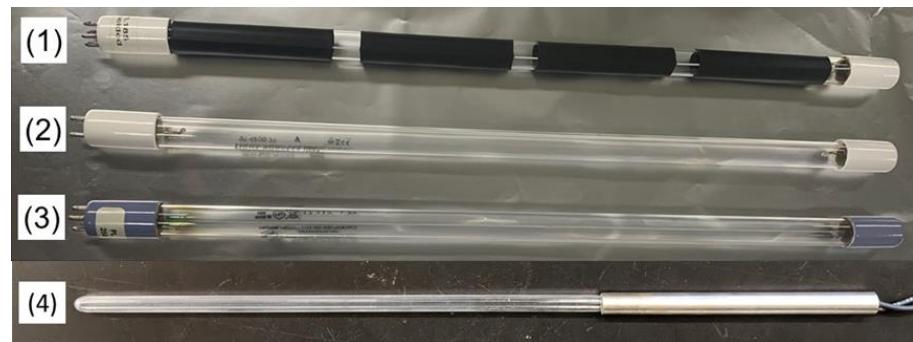
**Figure S2: Four types of lamps used in this research. Type (1) transmits both 185 and 254 nm radiation, with 80% surface covered with heat shrink tubes (GPH436T5VH/4, Light Sources, Inc.). Type (2) is the same as type (1) but not covered. Type (3) transmits only 254 nm radiation and is not covered (GPH436T5L/4, Light Sources, Inc.). Type (4) transmits both 185 and 254 nm radiation (model no. 82-9304-03, BHK Inc.).**

105
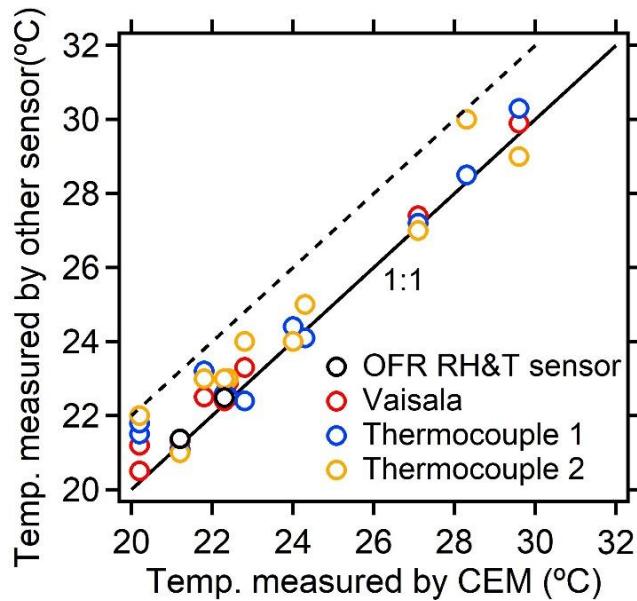
**Figure S3: Comparison between different temperature measurements used in this research. The measured temperatures from the CEM sensor, which was used to measure the room temperature, are shown on the x-axis. The Vaisala sensor is used to measure the temperature inside the OFR. Thermocouple 1 and Thermocouple 2 are used to measure the temperature of the OFR exhaust and outside surface. Detailed information about different sensors can be found in Table S1.**
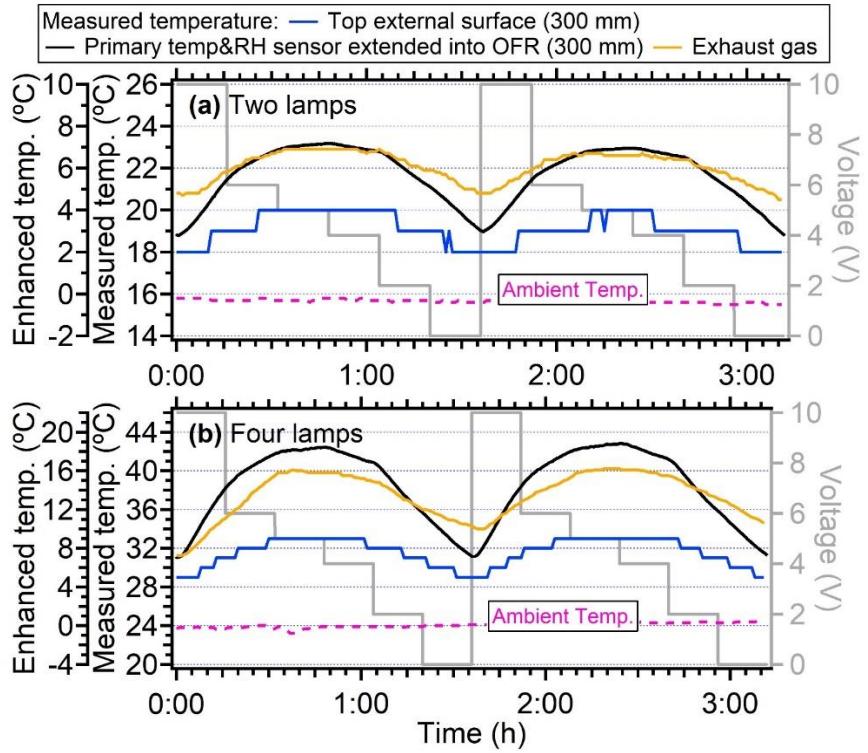
**Figure S4: Temperature variation for (a) four lamps and (b) two lamps. In this case, the front plate with a hexagon nut and mesh screen was installed, and the OFR sensor set in the backplate was extended into the center of OFR (probing depth: 300 mm). The mesh screen near the back plate was removed.**
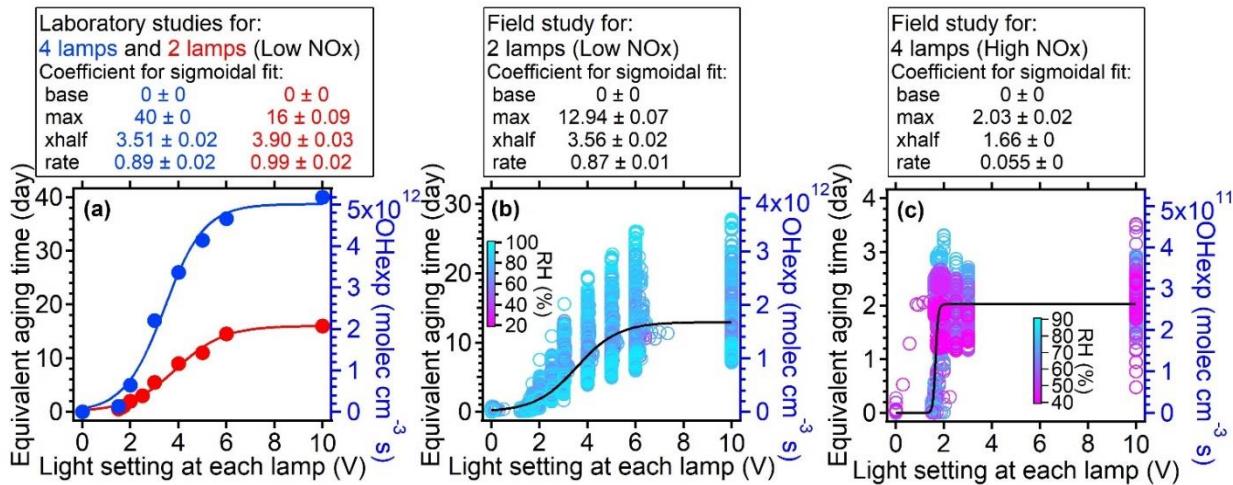
**Figure S5:** The correlation between OH exposures (right axis) and equivalent aging time (left axis) vs light settings at each lamp. A sigmoidal function was used to fit the scatter plots. The OH exposures under low NOx condition in panel (a) and (b) is estimated based on the empirical parameterization in Hu et al. (2022), while OH exposures in panel (c) under high NOx conditions is estimated based on the parameterization reported in Peng et al. (2018). A water mixing ratio of around 1.88% (60% RH at 25 °C) under low NOx conditions was assumed in the laboratory studies (Panel (a)). The mixing ratio in field studies (Panel (b) and (c)) was measured directly by RH&T sensor. The input flow rate is 5 L min$^{-1}$, which corresponds to a residence time of 167 s.
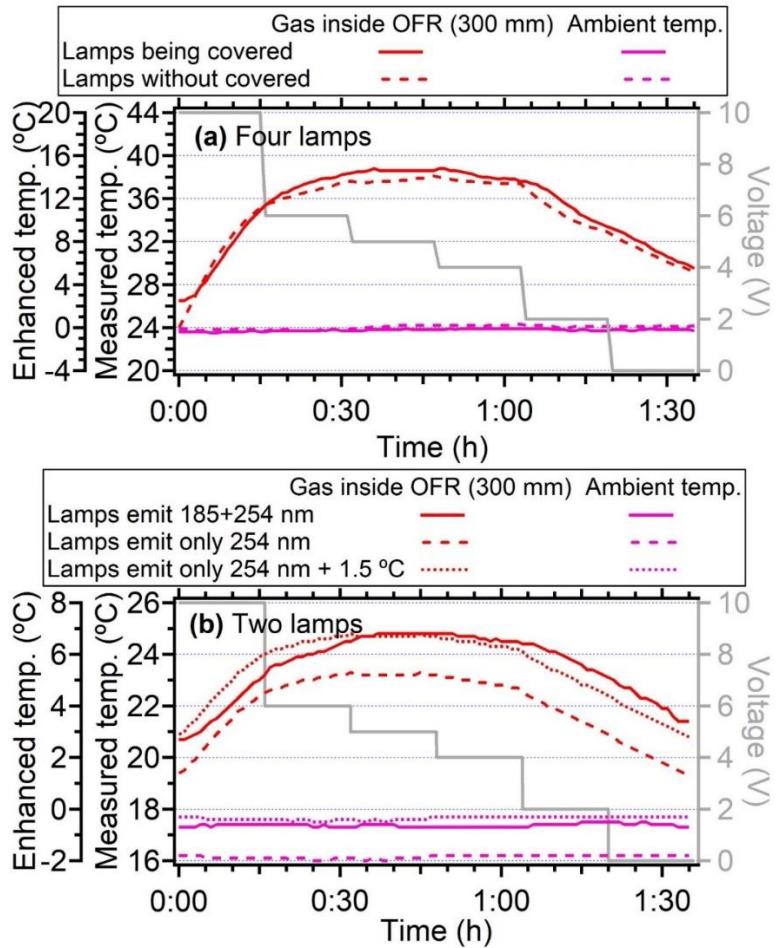
**Figure S6: The measured temperature variation with different types of Light Source lamps: (a) lamps with 80% surface covered with heat-shrink tubes and lamps without covered, (b) lamps emit both 185 and 254 nm radiation and lamps emit only 254 nm radiation.  The temperature of the gas inside OFR at a depth of 300 mm was measured.**
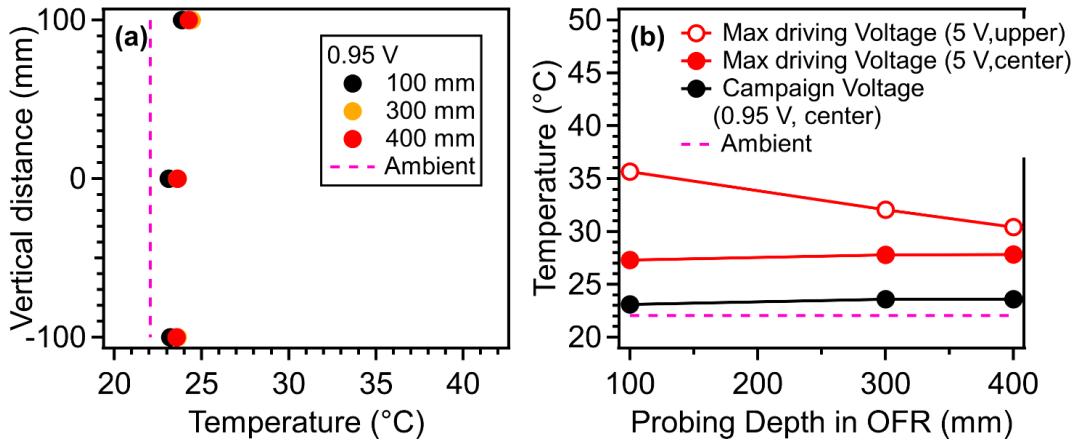
**Figure S7: Temperature measured by an external temperature sensor for an OFR with BHK lamps (a) in the vertical direction at different depths inside OFR, with the driving voltage set to 0.95 V for two lamps; (b) the measured temperature at different depths inside the OFR under different driving voltages; the "upper" indicates the position of 100 mm in the vertical direction and the "center" indicated the position measured at centerline. Flow through the OFR was 4.5 L min⁻¹.**
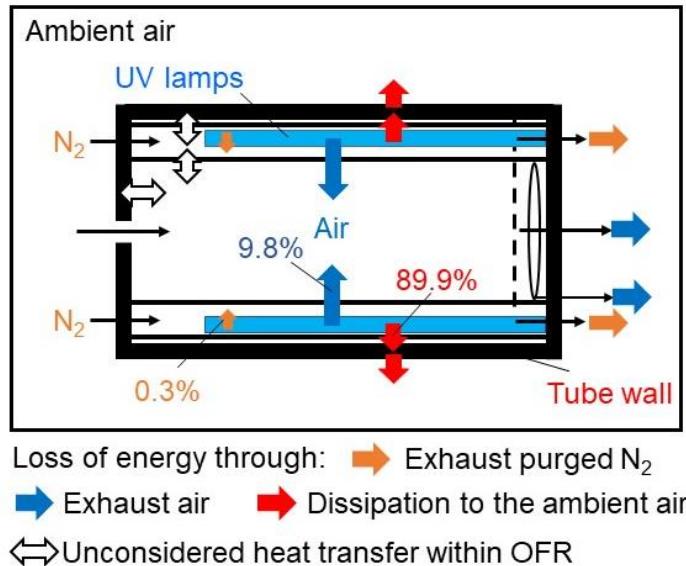
**Figure S8: Schematic plot for the transfer of the heating energy (orange arrows) inside the OFR from the UV lamps and the loss of energy (red arrows) to the ambient air. The fraction of energy from the UV lamps is obtained from Fig. S9. Note that only the power leading to the temperature increase (51% of total power, which is 35.6 W based on the calculation in Sec S1 and S2) of the OFR has been considered for these three pathways.**
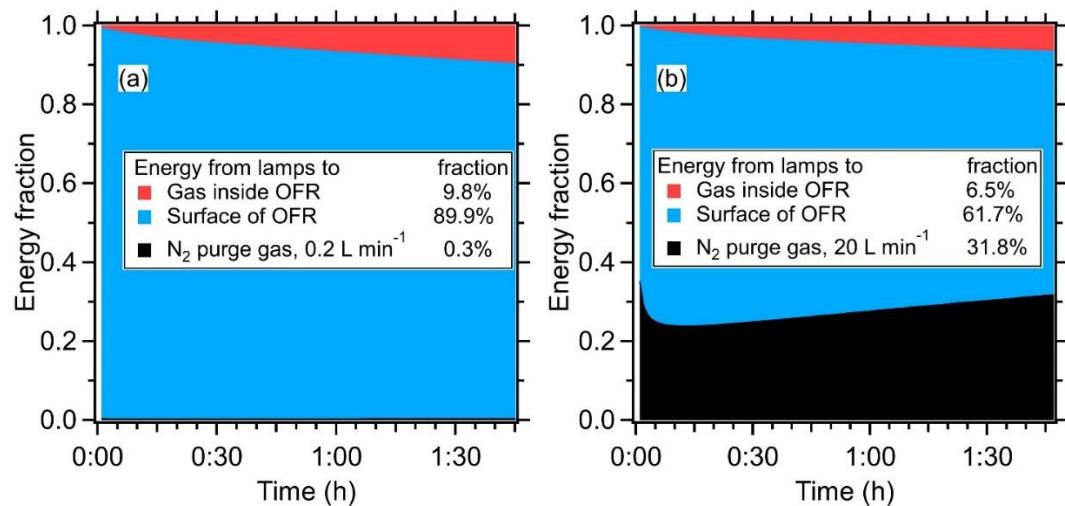
**Figure S9: (a) Energy from UV lamps (51% (based on calculation in Sect. S2) of total power (35.6 W), 8.9 W for each lamp, 4 lamps in total) to gas inside OFR, surface of OFR and $N_2$ purge gas (0.2 L $min^{-1}$) as a function of time, with 4 lamps set to 10 V. The start time is when the lamps are turned on. The flow rate is 5 L $min^{-1}$. (b) Same as Fig. S9a, with the flow rate of $N_2$ purge gas increased to 20 L $min^{-1}$. Details of the energy calculation are presented in Sect. S2.**

145
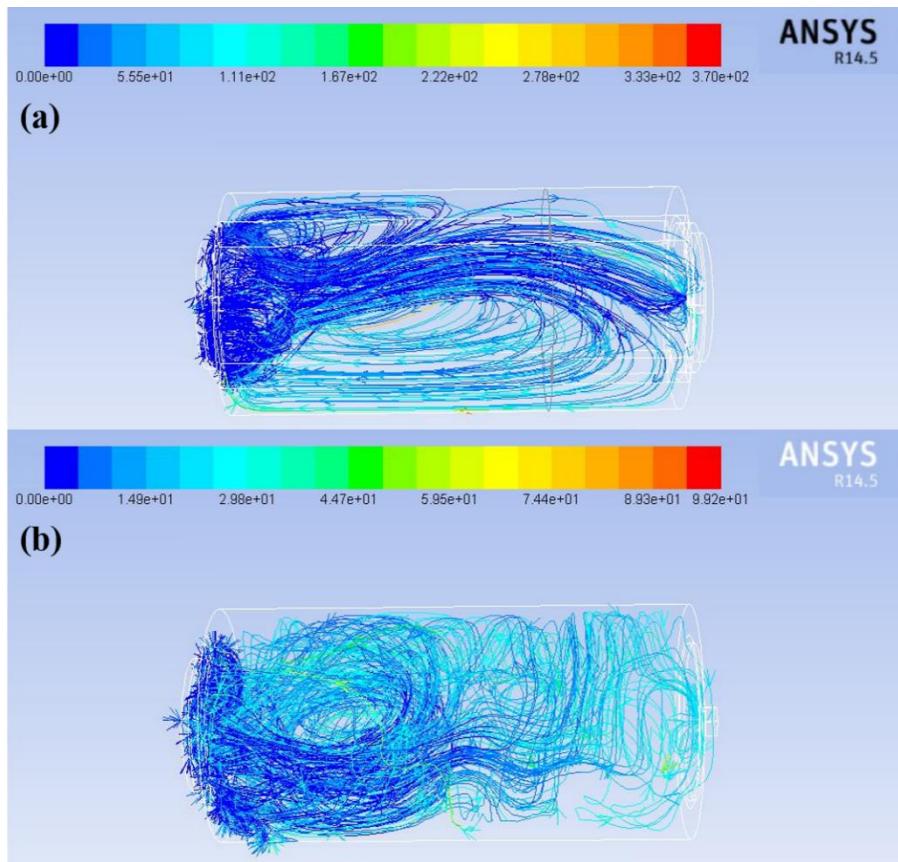
150

**Figure S10: CFD simulation of the gases in OFR (a) without and (b) with the heating of lamps. In panel (b), the scenario of four lamps at 5 V was simulated.**
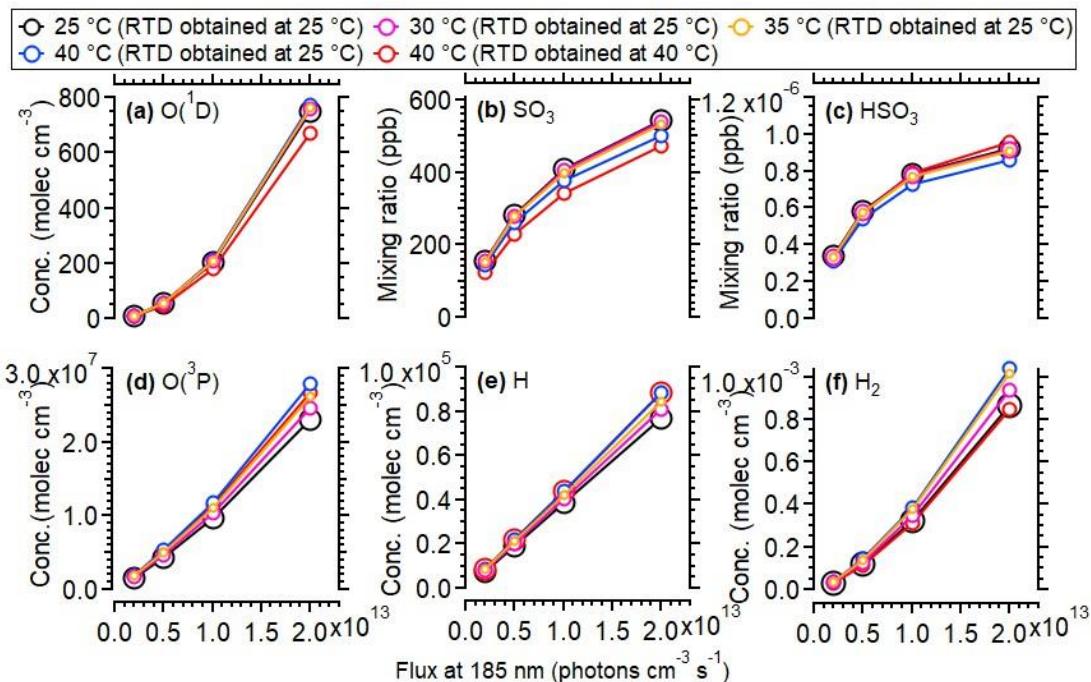
155 **Figure S11: Simulated concentration of oxidant species from 25 to 40 °C in OFR as a function of OH exposure. In this scenario, the 800 ppb of initial SO₂, 2.2% water vapor mixing ratio (25 °C, 70% RH), and different photon flux at 185 nm and 254 nm (photon flux ratio of 254/185 nm= 0.05) were used. The simulated oxidant concentrations with measured RTD in OFR were also shown.**

160
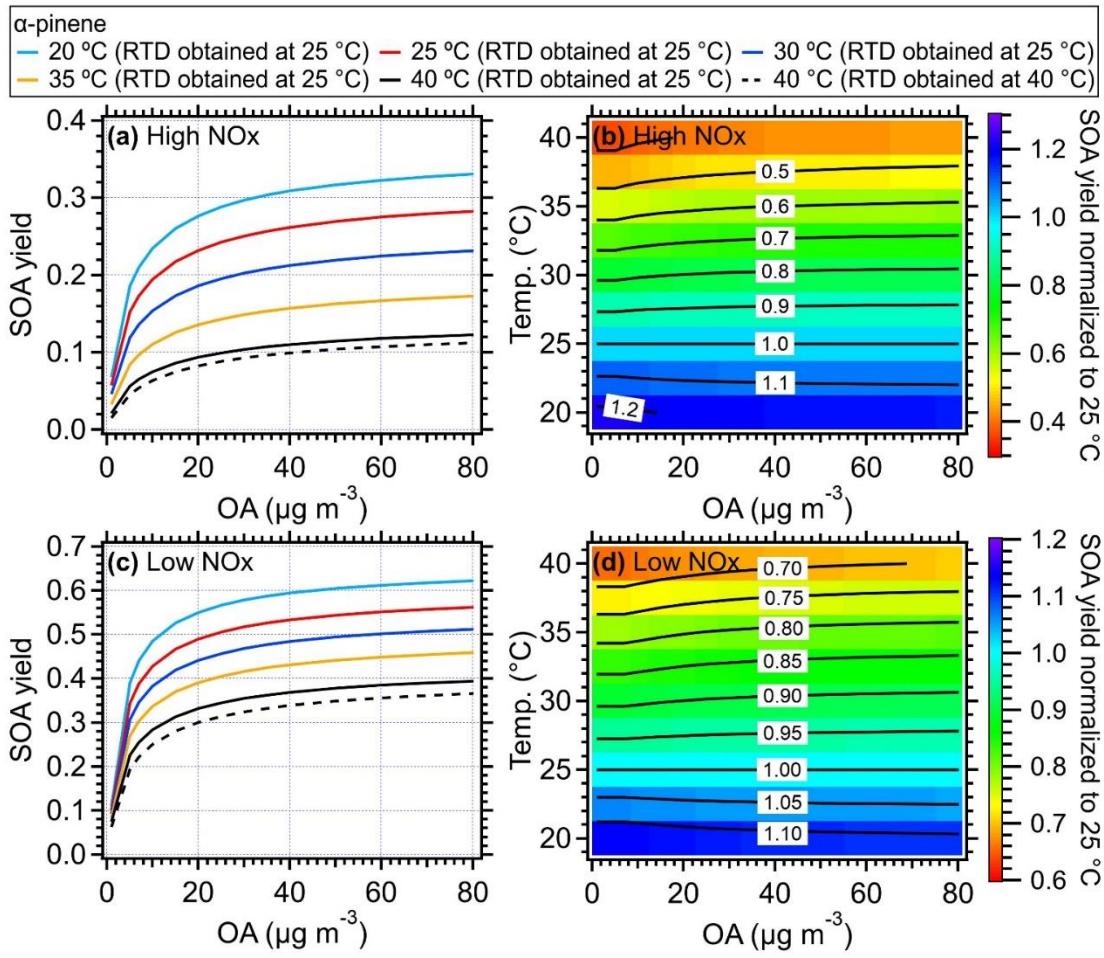
**Figure S12: Simulated SOA yield of α-pinene as a function of mass concentration of organic aerosol and temperature inside of the OFR for (a) high NOx and (c) low NOx conditions, respectively. The simulated results using measured RTD obtained at 40 °C are shown as black dashed lines. The ratio of SOA yield of α-pinene from different temperatures compared to that of 25 °C under (b) high NOx and (d) low NOx conditions. The equivalent aging time is 0.5 days by**

165 **assuming the OH concentration is equivalent to $1.5 \times 10^6$ molecule cm$^{-3}$ (Mao et al., 2009).**

**Figure S13: Simulated SOA yield of toluene as a function of mass concentration of organic aerosol and temperature inside of the OFR for (a) high NOx and (c) low NOx conditions, respectively. The simulated results using measured RTD obtained at 40 °C are shown as black dashed lines. The ratio of SOA yield of toluene from different temperatures compared to that of 25 °C under (b) high NOx and (d) low NOx conditions. The equivalent aging time is 1 day by assuming the OH concentration is equivalent to $1.5\times10^6$ molecule cm$^{-3}$ (Mao et al., 2009).**
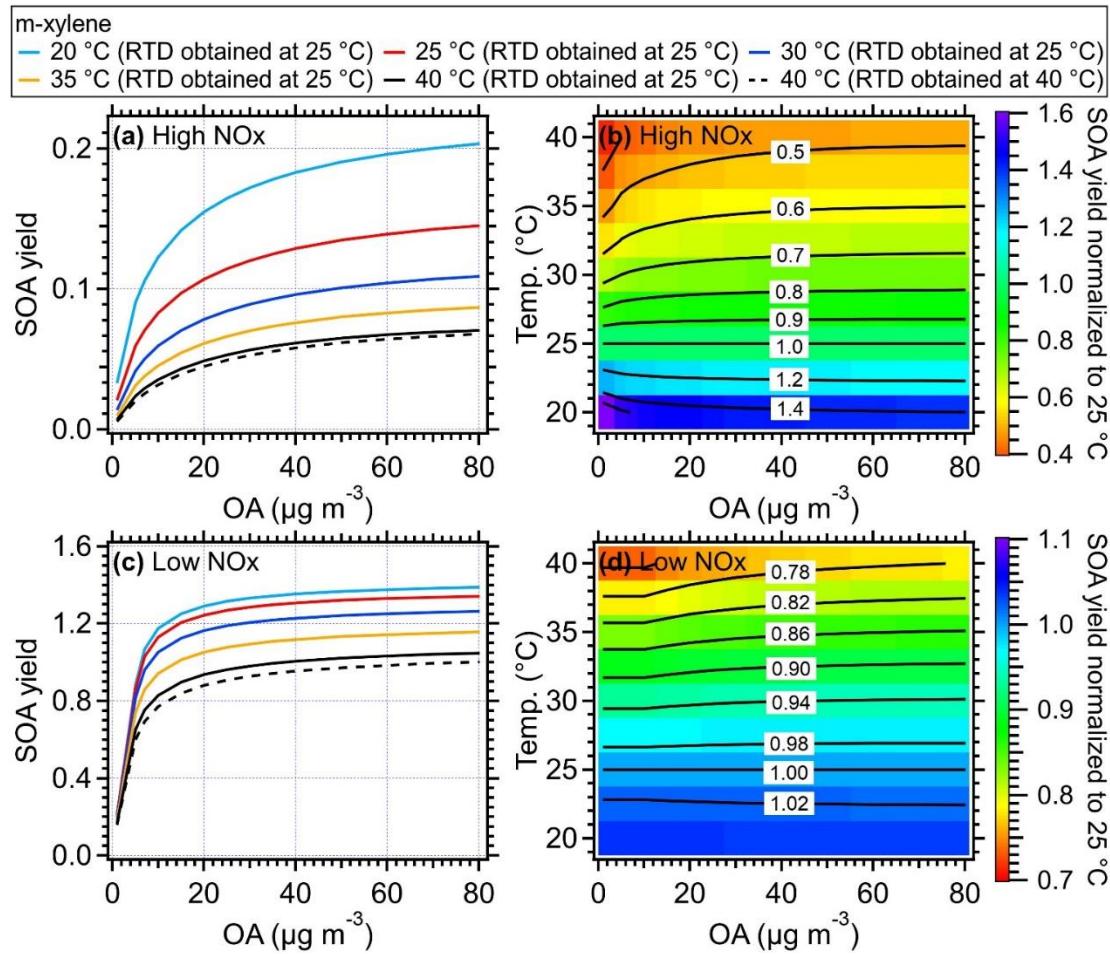
**Figure S14: Simulated SOA yield of xylene as a function of mass concentration of organic aerosol and temperature inside of the OFR for (a) high NOx and (c) low NOx conditions, respectively. The simulated results using measured RTD obtained at 40 °C are shown as black dashed lines. The ratio of SOA yield of xylene from different temperatures compared to that of 25 °C under (b) high NOx and (d) low NOx conditions. The equivalent aging time is 1 day by assuming the OH concentration is equivalent to $1.5\times10^6$ molecule cm$^{-3}$ (Mao et al., 2009).**
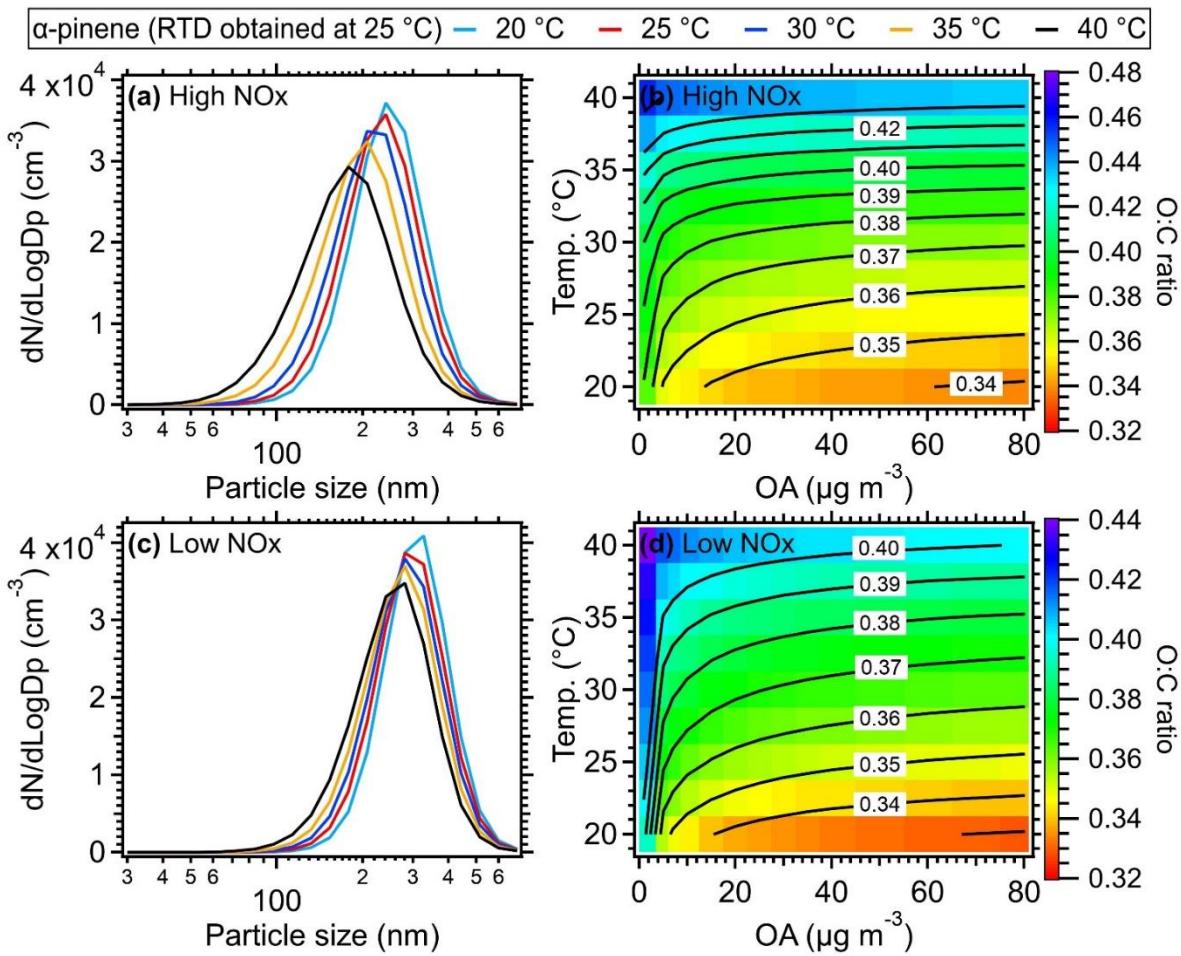
180

**Figure S15. Simulated size distribution of α-pinene as a function of temperature by assuming the mass concentration of OA is 30 μg m$^{-3}$ for (a) high NOx and (c) low NOx conditions, respectively. Simulated O: C ratio of α-pinene under different temperatures and organic aerosol concentrations under (b) high NOx and (d) low NOx conditions. The equivalent aging time is 0.5 days by assuming the OH concentration is equivalent to 1.5×10$^6$ molec cm$^{-3}$ (Mao et al.,**
185  **2009).**
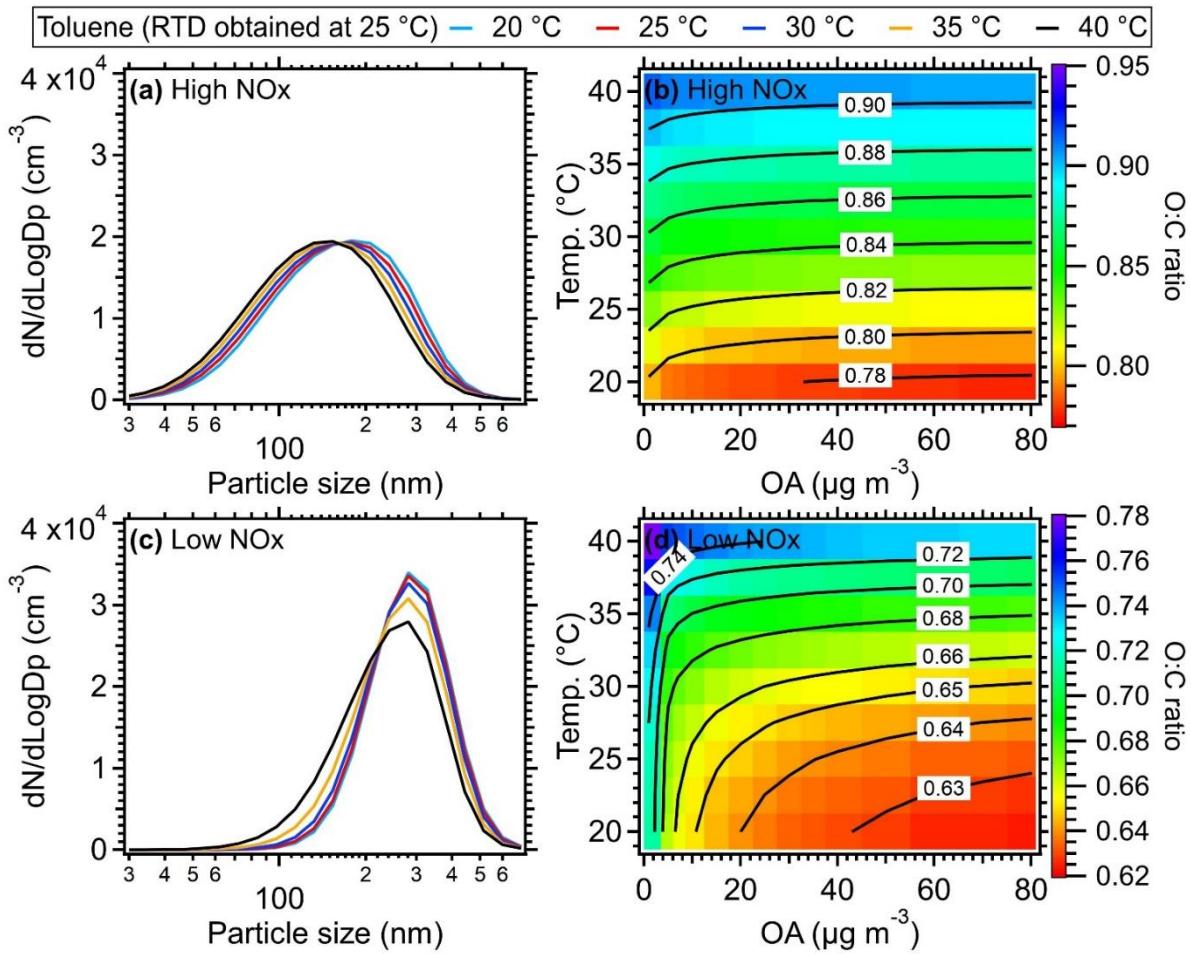
**Figure S16: Simulated size distribution of toluene as a function of temperature by assuming the mass concentration of OA is 30 μg m⁻³ for (a) high NOx and (c) low NOx conditions, respectively. Simulated O:C ratio of toluene under different temperature and organic aerosol concentration under (b) high NOx and (d) low NOx conditions. The equivalent aging time is 1 day by assuming the OH concentration is equivalent to 1.5×10⁶ molecule cm⁻³ (Mao et al., 2009).**

190
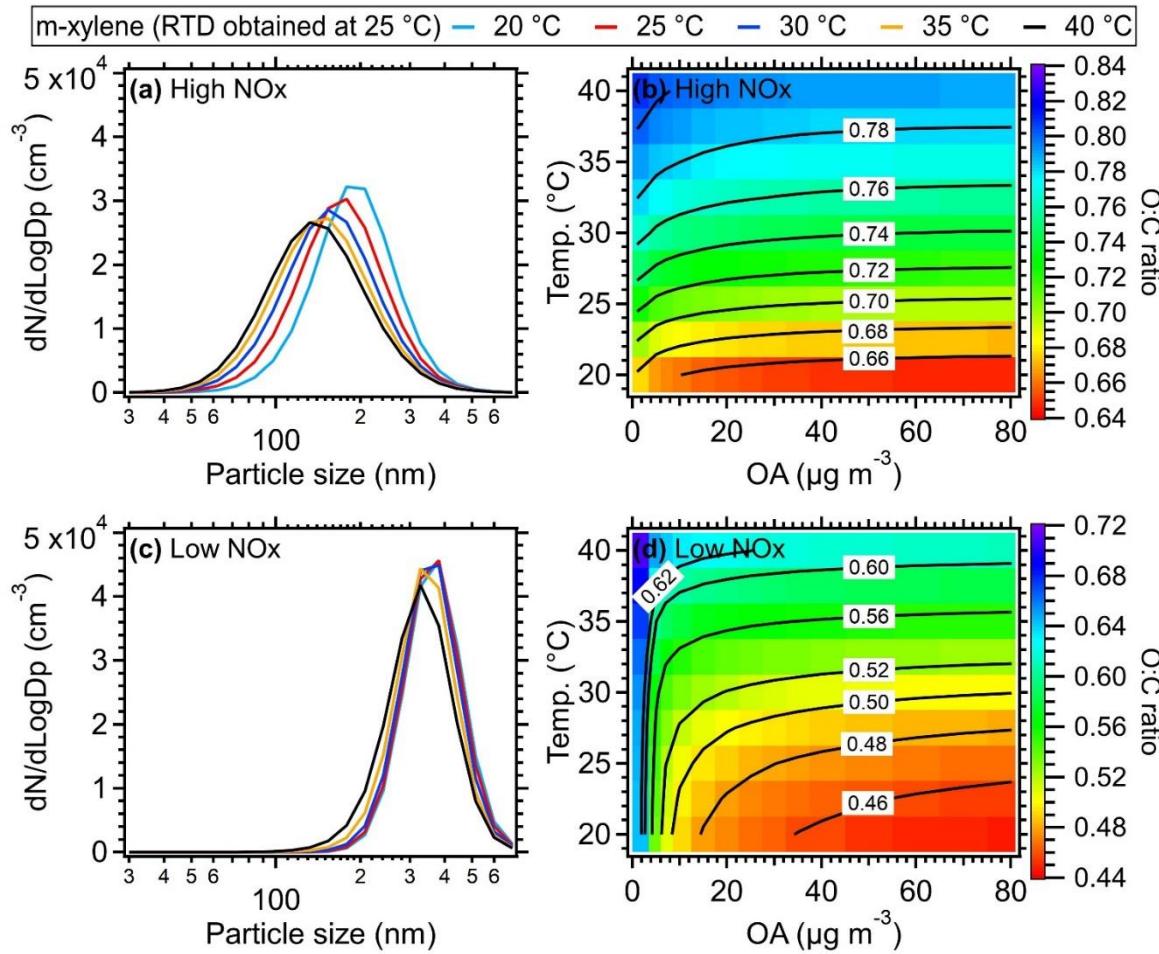
**Figure S17**: **Simulated size distribution of m-xylene as a function of temperature by assuming the mass concentration**
**of OA is 30 µg m$^{-3}$ for (a) high NOx and (c) low NOx conditions, respectively. Simulated O:C ratio of m-xylene under**
**different temperatures and organic aerosol concentration under (b) high NOx and (d) low NOx conditions. The**
**equivalent aging time is 1 day by assuming the OH concentration is equivalent to 1.5×10$^6$ molecule cm$^{-3}$ (Mao et al.,**
**2009).**

200
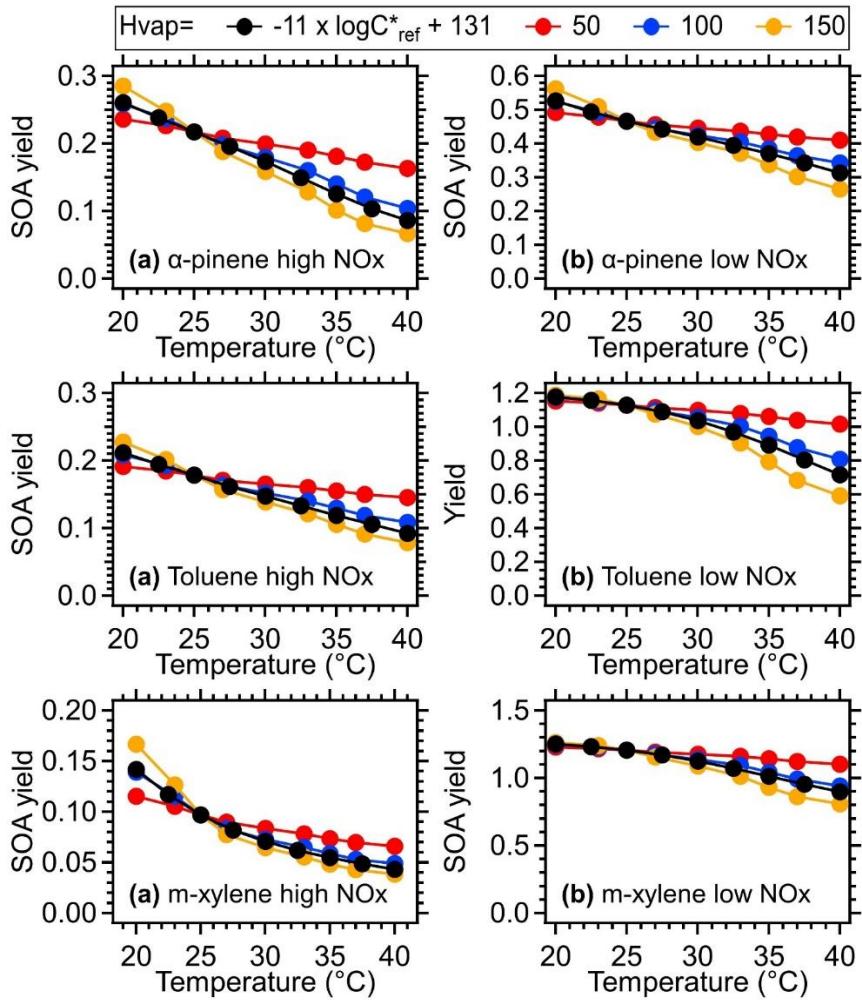
**Figure S18: Simulated SOA yield of (a-b) α-pinene, (c-d) Toluene, (e-f) m-xylene as a function of temperature under different $H_i^{vap}$ values. The mass concentration of organic aerosol is assumed to be 15 μg m⁻³. The equivalent aging time is 1 day assuming the OH concentration is equivalent to 1.5×10⁶ molecule cm⁻³ (Mao et al., 2009).**
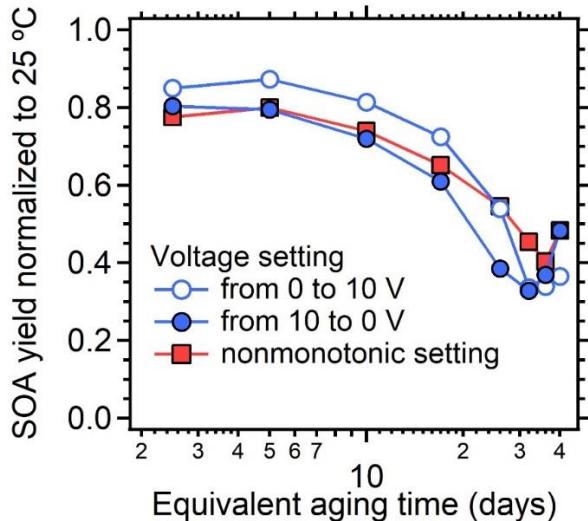
205

**Figure S19. Simulated ratio of SOA yield with measured temperature vs that under 25 °C under varied lamp settings. A 10-ppb toluene with OA mass concentration of 30 μg m⁻³ was assumed. The equivalent aging time is calculated by assuming the OH concentration is equivalent to $1.5 \times 10^6$ molecule cm⁻³ (Mao et al., 2009).**

## References

Bianchi, F., Kurten, T., Riva, M., Mohr, C., Rissanen, M. P., Roldin, P., Berndt, T., Crounse, J. D., Wennberg, P. O., Mentel, T. F., Wildt, J., Junninen, H., Jokinen, T., Kulmala, M., Worsnop, D. R., Thornton, J. A., Donahue, N., Kjaergaard, H. G., and Ehn, M.: Highly Oxygenated Organic Molecules (HOM) from Gas-Phase Autoxidation Involving Peroxy Radicals: A Key Contributor to Atmospheric Aerosol, Chem Rev, 119, 3472-3509, https://doi.org/10.1021/acs.chemrev.8b00395, 2019.

Cappa, C. D., Zhang, X., Loza, C. L., Craven, J. S., Yee, L. D., and Seinfeld, J. H.: Application of the Statistical Oxidation Model (SOM) to Secondary Organic Aerosol formation from photooxidation of of C12 alkanes, Atmospheric Chemistry and Physics, 13, 1591-1606, https://doi.org/10.5194/acp-13-1591-2013, 2013.

Chhabra, P. S., Ng, N. L., Canagaratna, M. R., Corrigan, A. L., Russell, L. M., Worsnop, D. R., Flagan, R. C., and Seinfeld, J. H.: Elemental composition and oxidation of chamber organic aerosol, Atmospheric Chemistry and Physics, 11, 8827-8845, https://doi.org/10.5194/acp-11-8827-2011, 2011.

Epstein, S. A., Riipinen, I., and Donahue, N. M.: A semiempirical correlation between enthalpy of vaporization and saturation concentration for organic aerosol, Environ Sci Technol, 44, 743-748, https://doi.org/10.1021/es902497z, 2010.

Holman, J. P.: Heat Transfer, 10 edn, McGraw-Hill, New York, USA, 2010.

Hu, W., Zhou, H., Chen, W., Ye, Y., Pan, T., Wang, Y., Song, W., Zhang, H., Deng, W., Zhu, M., Wang, C., Wu, C., Ye, C., Wang, Z., Yuan, B., Huang, S., Shao, M., Peng, Z., Day, D. A., Campuzano-Jost, P., Lambe, A. T., Worsnop, D. R., Jimenez, J. L., and Wang, X.: Oxidation Flow Reactor Results in a Chinese Megacity Emphasize the Important Contribution of S/IVOCs to Ambient SOA Formation, Environ Sci Technol, 56, 6880-6893, https://doi.org/10.1021/acs.est.1c03155, 2022.

Huang, Y., Coggon, M. M., Zhao, R., Lignell, H., Bauer, M. U., Flagan, R. C., and Seinfeld, J. H.: The Caltech Photooxidation Flow Tube reactor: design, fluid dynamics and characterization, Atmospheric Measurement Techniques, 10, 839-867, https://doi.org/10.5194/amt-10-839-2017, 2017.

Loza, C. L., Craven, J. S., Yee, L. D., Coggon, M. M., Schwantes, R. H., Shiraiwa, M., Zhang, X., Schilling, K. A., Ng, N. L., Canagaratna, M. R., Ziemann, P. J., Flagan, R. C., and Seinfeld, J. H.: Secondary organic aerosol yields of 12-carbon alkanes, Atmospheric Chemistry and Physics, 14, 1423-1439, https://doi.org/10.5194/acp-14-1423-2014, 2014.

Mao, J., Ren, X., Brune, W. H., Olson, J. R., Crawford, J. H., Fried, A., Huey, L. G., Cohen, R. C., Heikes, B., Singh, H. B., Blake, D. R., Sachse, G. W., Diskin, G. S., Hall, S. R., and Shetter, R. E.: Airborne measurement of OH reactivity during INTEX-B, Atmospheric Chemistry and Physics, 9, 163-173, https://doi.org/10.5194/acp-9-163-2009, 2009.

Ng, N. L., Kroll, J. H., Chan, A. W. H., Chhabra, P. S., Flagan, R. C., and Seinfeld, J. H.: Secondary organic aerosol formation from m-xylene, toluene, and benzene, Atmospheric Chemistry and Physics, 7, 3909-3922, https://doi.org/10.5194/acp-7-3909-2007, 2007.

Peng, Z., Palm, B. B., Day, D. A., Talukdar, R. K., Hu, W., Lambe, A. T., Brune, W. H., and Jimenez, J. L.: Model Evaluation of New Techniques for Maintaining High-NO Conditions in Oxidation Flow Reactors for the Study of OH-Initiated Atmospheric Chemistry, ACS Earth and Space Chemistry, 2, 72-86, https://doi.org/10.1021/acsearthspacechem.7b00070, 2018.

Zhang, X., Cappa, C. D., Jathar, S. H., McVay, R. C., Ensberg, J. J., Kleeman, M. J., and Seinfeld, J. H.: Influence of vapor wall loss in laboratory chambers on yields of secondary organic aerosol, Proc Natl Acad Sci U S A, 111, 5802-5807, https://doi.org/10.1073/pnas.1404727111, 2014.